Larrayoz Izcara, X.; Guirao Blank, A.; Pyczak, F.; Staron, P.; Schumann, S.; Huber, N.:

Characterization and modeling of the influence of artificial aging on the microstructural evolution of age-hardenable AlSi10Mg(Cu) aluminum alloys

In: Materials Science and Engineering A (2014) Elsevier

DOI: 10.1016/j.msea.2014.04.031

Characterization and modeling of the influence of artificial ageing on the microstructural evolution of age–hardenable $AlSi_{10}Mg(Cu)$ aluminum alloys

X. Larráyoz Izcara[a,1], A. Guirao Blank[a], F. Pyczak[b], P. Staron[b], S. Schumann[a], N. Huber[b]

[a] Department of Materials, Group Research, Volkswagen AG, Berliner Ring 2, 38436 Wolfsburg, Germany

[b] Institute of Materials Research, Helmholtz–Zentrum Geesthacht Center for Materials and Coastal Research, Max Planck–Str. 1, 21502 Geesthacht, Germany

[1] Department of Vehicle Body Development, Technical Centre, SEAT SA, Carretera N-II km. 585, 08760 Martorell, Spain

Corresponding author:

Mr. Norbert Huber

Max–Planck–Straße 1, 21502 Geesthacht, Germany

☎ +49 4152 87-2500

FAX +49 4152 87-42501

✉ norbert.huber@hzg.de

1 Abstract

A comprehensive analysis of the effect of the artificial ageing stage of the precipitation heat treatment T_6–T_7 process on the microstructure of the age–hardenable $AlSi_{10}Mg(Cu)$ aluminum alloy is presented that considers the influence of temperature and time of the ageing conditions on the formation and evolution of the Mg_2Si strengthening precipitate distributions. A complete quantitative characterization of the strengthening distributions covering a broad range of ageing conditions was obtained using the small angle neutron scattering (SANS) technique, complemented with transmission electron microscopy (TEM) and high–resolution transmission microscopy (HTEM). This information was successfully used to fit Robson's precipitation model for the coupled nucleation, growth, and coarsening of Mg_2Si strengthening precipitates. A unique set of modeling parameters was obtained for the whole precipitation process. Robson's model is shown to be a powerful tool for predicting the evolution of these nanometer–scale particles in industrial and complex ageing processes, which are critical for designing new components based on the material requirements.

Keywords: Aluminum alloy, Precipitation strengthening, Ageing, Small Angle Neutron Scattering, Modeling

2 Introduction

The literature has established that the macromechanical performance of age–hardenable alloys is defined by the size distribution of their strengthening precipitates [1–4]. Al–Si–Mg alloys are typical examples of this type of material. These alloys are commonly used in the automobile sector to produce different components [5]. The investigated alloy in this report is the $AlSi_{10}Mg(Cu)$. The composition of the alloy is given in Table 1. In this case, the material strengthening occurs because of the formation of Mg_2Si precipitate distributions during the T_6 heat treatment process [6–9].

Si	Mg	Sr	Ti	Fe	Cu	Zn	Mn
10.0–11.0	0.35–0.50	max. 0.05	0.05–0.15	max. 0.55	max. 0.3	max. 0.3	0.2–0.5

Table 1: The chemical composition of the alloy VDS 233 $AlSi_{10}Mg(Cu)$.

A T_6 heat treatment is a precipitation process in which a fine distribution of a hardening phase is created under specific and controlled temperature and time conditions to interact with dislocations to produce the desired material strengthening [10, 11]. In brief, this type of heat treatment starts with a solution treatment at a high temperature to create a supersaturated solid solution state (SSSS) of the alloy. After water quenching at room temperature, the SSSS decomposes, creating a homogeneous size distribution of strengthening precipitates during the artificial ageing process. Mg_2Si precipitates nucleate first in the form of metastable and coherent β'' phases [12]. This initial precipitate distribution does not strengthen significantly the material [11]. However, if the duration of ageing is increased, the evolution of this distribution to the metastable and semi–coherent β' phase produces the maximum strengthening of the material [12]. For a sufficient ageing time, a total incoherent distribution of the stable β phase is finally obtained [12], which lowers the strength of the material as the duration of the artificial ageing increases [13](Fig. 1). Increasing the ageing temperature accelerates the precipitation process and produces a coarser distribution [10, 11].

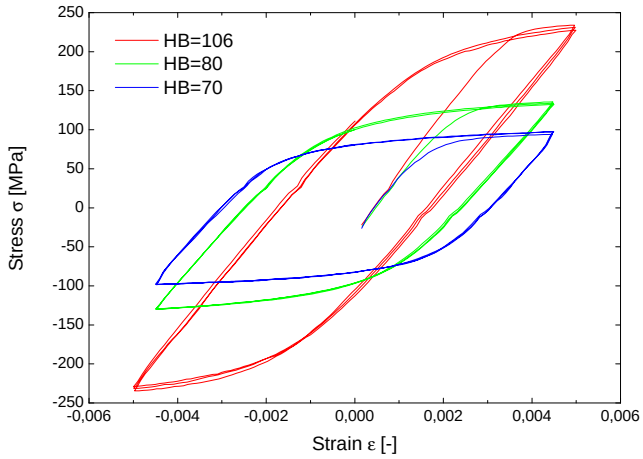

Figure 1: Stress–strain curves from the three first cycles of low cycle fatigue (LCF) tests performed at 250°C for three different hardness states, i.e., ageing conditions. HB denotes the Brinell hardness. Higher hardness states correspond to shorter ageing durations.

Although the size, shape, and approximate composition of the Mg_2Si strengthening precipitates of this alloy [14–17], as well as the precipitation sequence [12] and the strengthening mechanisms [13, 18] have been well–established in the literature, the influence of the ageing conditions of the T_6 precipitation hardening process on the formation of the Mg_2Si strengthening distributions is not fully established [1, 2, 9]. Additionally, the size distribution of the Mg_2Si strengthening precipitates created in the material has not been quantified. Small angle neutron scattering (SANS) investigations, complemented with transmission electron microscopy (TEM) and high–resolution transmission microscopy (HTEM), is an ideal option for deriving valuable and statistically meaningful experimental information about the strengthening distributions obtained according to different temperature and duration ageing conditions. The investigations in this work are focused exclusively on the artificial ageing process and the equilibrium β–Mg_2Si precipitates. Thus, the heat treatment should be denoted as a T_7 process because the so–called over–ageing stage is of great interest.

Despite successful quantitative characterization of the size distributions of the Mg_2Si strengthening precipitates at various temperatures and durations of the ageing process, the effect of the variation of the ageing conditions on the size distributions cannot be quantitatively predicted. Moreover, the experimental characterization of multi–stage or complex ageing processes are also costly and endless. For these reasons, data from the SANS and TEM investigations are used to fit Robson's precipitation model for the Mg_2Si strengthening precipitate distributions [3, 19–22]. This model predicts the size distributions of the Mg_2Si strengthening precipitates in both one– and multi–stage artificial ageing processes over a large range of ageing temperatures as well as the whole precipitation sequence from the early nucleation to the final coarsening processes for a unique set of model parameters [22]. Adapting Robson's model will allow it to be applied for designing and optimizing the artificial ageing processes in an industrial setting to achieve the required mechanical properties for the $AlSi_{10}Mg(Cu)$ alloy.

3 Microstructure Analysis

The information obtained about the dendrite arm spacing (DAS) of the aluminium matrix dendrites; length, orientation, and form of the Al_5FeSi needles; and size and circularity of the eutectic silicon particles are provided in the following sections. Some comments about other less common intermetallic precipitates present in the microstructure configuration of Al–Si–Mg alloy systems are also included.

3.1 Sample preparation

The secondary alloy for this study was melted in an electric furnace at 730°C and was then poured into metallic molds pre–heated at 200°C. Once the gate system was removed, bars of 270 mm in length and 23 mm in diameter were obtained. Prior to heat treatment, disc–shaped samples of 10 mm in thickness were prepared from the same bar. All samples were solution treated at 535°C for 6 hours followed by quenching in water at room temperature.

The samples were then artificially aged at two different temperatures. A temperature of 210°C was used to create samples aged until they reached the early stages of nucleation and were close to the peak hardening, while samples aged at 280°C provided over–aged states. The time between the quenching stage and the beginning of the artificial ageing is critical because this alloy can also precipitate at room temperature, forming small clusters of silicon and magnesium [12]. This time gap is limited to a maximum of 10 minutes. Table 2 lists the different ageing temperature and duration conditions for the seven experimental states and their corresponding hardness measurements.

The following discussion is based on results obtained for states II and VII, corresponding to the peak–aged and the long over–aged states, respectively.

State	Hardness	Ageing Conditions	
		T_{ageing}	t_{ageing}
	HBW 2.5/62.5/20	°C	h
I	119.4	210	0.2
II	124.8	210	0.5
III	108.2	210	2.0
IV	84.0	280	0.5
V	63.7	280	19.0
VI	56.1	280	69.0
VII	50.1	280	211.0

Table 2: The microstructure and collecting hardness values as well as the temperature and length of the artificial ageing process for selected ageing states are listed. The designation "HBW 2.5/62.5/20" for hardness specifies the use of a tungsten carbide ball indenter for the Brinell test with a diameter of 2.5 mm applying a 62.5 kgf force maintained for 20 s.

3.2 Dendrite Arm Spacing (DAS)

All aluminum alloy castings exhibit a characteristic dendritic solidification microstructure [23]. The effect of dendrite arm spacing on the mechanical properties of aluminum alloy industrial components has been extensively studied [24].

The results for the peak–aged and long over–aged samples are shown in Figs. 2(a) and 2(b). Here, the variation in the DAS scale in the whole ageing stage is not relevant.

Any change in the DAS is expected to occur during the solution heat treatment or quenching stages [6]. The spacing between adjacent arms in the dendrites is mainly determined by the solidification and cooling stages in the casting process, but is also influenced by the solute content [23]. The DAS decreases with decreased solidification time [23].

The results of the dendrite arm spacing (DAS) measurements are presented in Table 3. The spacing between dendrite arms influences the mechanical properties of the $AlSi_{10}Mg(Cu)$ alloy. However, it is not responsible

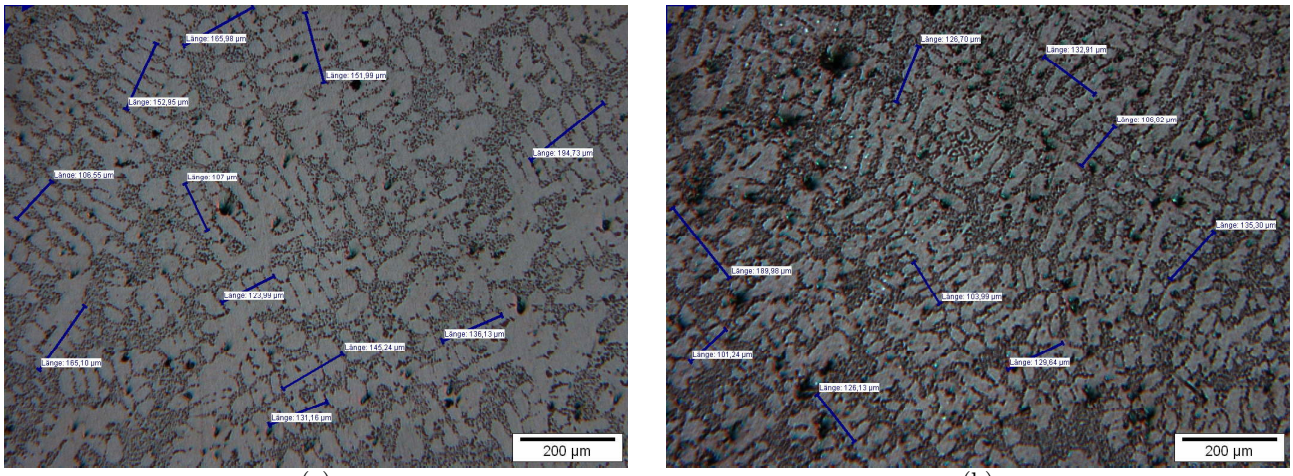

(a) (b)

Figure 2: Micrographs showing the DAS measurements: (a) for the peak–aged state; (b) for the long over–aged state. The DAS is not altered during the artificial ageing process.

for the observed variation in the mechanical performance of the material because it does not change during the ageing process.

Sample	DAS	Si eutectic	Al_5FeSi
	μm	μm	μm
I	22.90	1.63	24.34
II	22.53	1.64	12.00
III	19.81	1.70	6.13
IV	21.02	1.53	18.16
V	22.36	1.55	8.48
VI	22.76	1.79	9.81
VII	22.67	1.57	16.22

Table 3: Results of the DAS measurements, the average diameter of the silicon eutectic particles, and the length of the Al_5FeSi needles for the seven ageing states are presented. The roundness ratio of the silicon eutectic is approximately 80%.

3.3 Eutectic silicon particles

Alloys containing an excess of silicon above the stoichiometrically required amount to form Mg_2Si strengthening precipitates exhibit a modified composition and density of the particles [13] and preferentially form additional phases during the latter stages of ageing. However, this excess of silicon does not contribute significantly to the material strengthening [25].

The required characteristics to describe a silicon particle distribution are particle size, shape, and spacing. Figs. 3(a) and 3(b) show that the size and roundness of the eutectic silicon particles do not change during the artificial ageing process. The silicon eutectic sizes are shown in Table 3. The roundness ratio R is a parameter defined inside the image analysis software used, which is linked to the area A of the analyzed particle and the

longest distance between two points in the perimeter of the particle L and is calculated as shown in Eq. (1). A roundness value close to 100% is characteristic of spherically–shaped particles. In this study, the roundness of the silicon particles is approximately 80%.

$$R = \frac{4A}{\pi L} \cdot 100 \ . \tag{1}$$

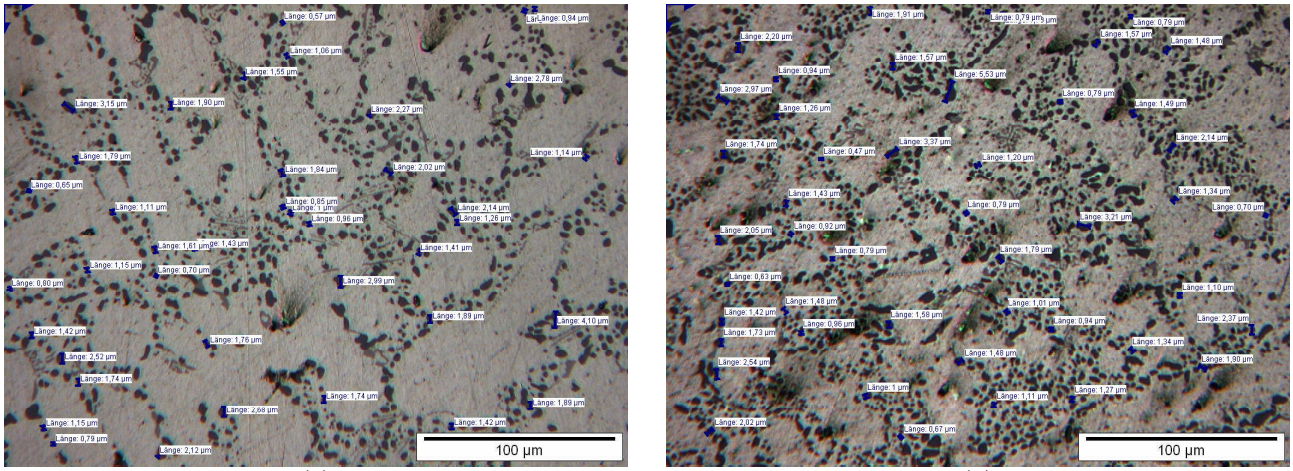

(a) (b)

Figure 3: Micrographs showing Si particles: (a) for the peak–aged state; (b) for the long over–aged state. The size of the eutectic particles remains unchanged.

In fact, the silicon particles are altered during solution heat treatment at 535°C prior to the ageing process. The fibrous morphology of eutectic silicon upon solidification is transformed into spherical particles due to the addition of a strontium chemical modifier to the chemical composition of the alloy. During the solution heat treatment stage, the well–known spheroidization process of the silicon particles also occurs. Eutectic silicon particles coarsen during the 6 hours solution heat treatment phase due to the Ostwald ripening phenomenon, thereby reducing the total interfacial energy between the aluminum matrix and the silicon particles [6]. Fig. 4 shows two micrographs that depict the remarkable effect of the solution treatment on the morphology of the silicon particles.

The eutectic silicon particles contribute to the global strengthening of the material and must be considered [25]. However, because there is no change in the size, spacing, or roundness of these precipitates during the ageing process (Table 3), just as observed for the dendrite arm spacing, the eutectic silicon particles are eliminated as a cause for the change in the mechanical properties of the alloy [25].

3.4 Al_5FeSi needles

Adding iron to the $AlSi_{10}Mg(Cu)$ alloy for chill–casted components is not preferable because it causes the material to become more brittle [23, 26]. The iron content comes from the secondary nature of the alloy. This element content forms different Fe intermetallic precipitates, such as the Chinese script $Al_{15}(MnFe)_3Si_2$ and $Al_8Mg_3FeSi_6$ phases, but most Fe is present in the form of Al_5FeSi needles (shown in Fig. 5).

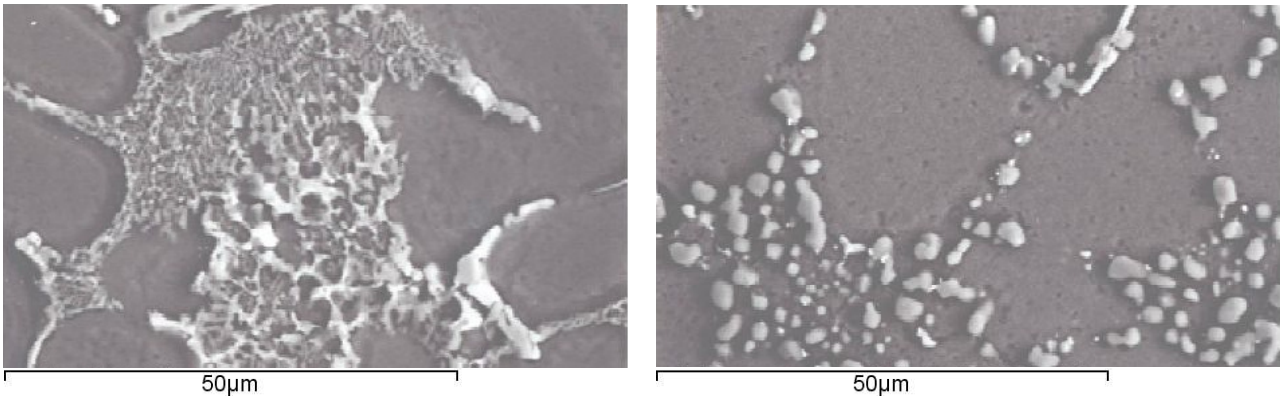

(a) (b)

Figure 4: Micrographs showing eutectic silicon particles in the interdendritic area: (a) at the as–cast state prior to heat treatment (fibrous morphology); (b) after solution heat treatment and prior to the ageing stage (spheroidal morphology).

The length of these Al_5FeSi needles is mostly determined during the solidification and cooling stage of the casting process. The slower the cooling rate after melting, the longer the needles become. Compared to the analyzed intermetallic phases, the length of the Al_5FeSi needles is remarkably scattered, even for measurements performed for the same state in different samples. However, no trend is observed, and the variation in length is completely random, suggesting an inhomogeneous distribution of iron in the casted material because, to some extent, these Al_5FeSi needles have not homogeneously precipitated in the interdendritic zone.

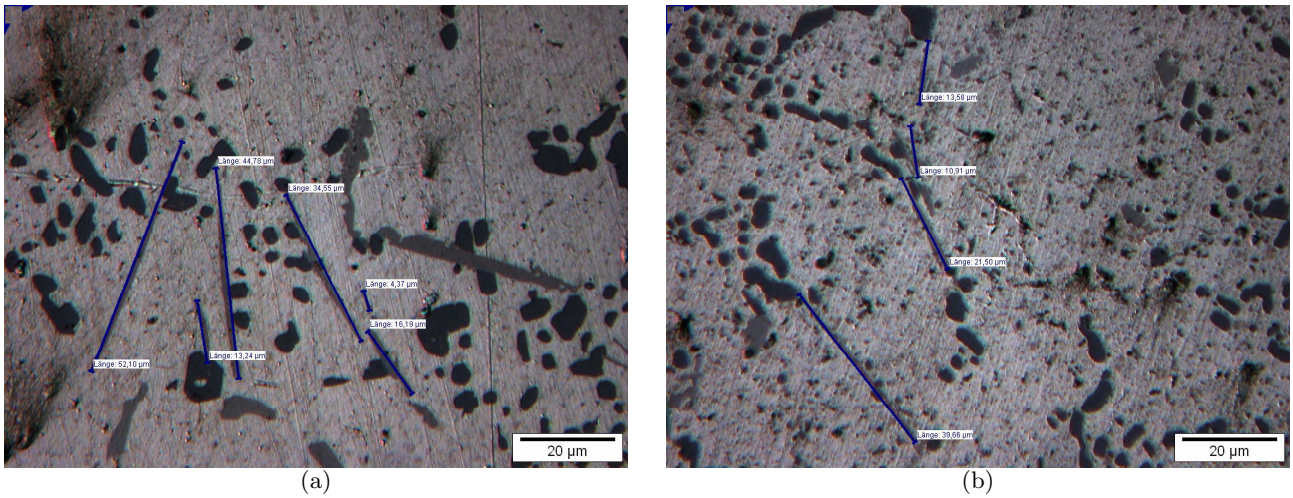

(a) (b)

Figure 5: Micrographs showing Al_5FeSi needles with scattering lengths: (a) for the peak–aged state; (b) for the long over–aged state.

Additionally, at the solution heat treatment stage, the $Al_8Mg_3FeSi_6$ phase decomposes slowly to release magnesium into the solution, which causes more β–Mg_2Si strengthening precipitates to nucleate and coarsen [13]. This decomposition produces very fine iron–rich precipitates, probably of the Al_5FeSi phase [6], which explains why the typical Chinese script form $Al_8Mg_3FeSi_6$ precipitates in the as–cast state have almost disappeared at any ageing state.

A partial dissolution of the original Al_5FeSi phase formed in the casting process during solution treatment

may be expected [6]. The dissolution of this phase occurs by decomposition of the Al_5FeSi into Al_6Fe and Si particles. Excess silicon then contributes to the Mg_2Si strengthening precipitates and may also explain the scattered length measurements of the Al_5FeSi needles.

The intermetallic Al_5FeSi phase in which the majority of the iron content is present is not considered as a key factor in explaining the change in the alloy's mechanical properties because there is no systematic trend in the change of the length of the Al_5FeSi needles, as shown in Table 3. Regardless, its presence in the material causes an undesirable embrittlement of the material.

4 Characterization of the Mg_2Si strengthening precipitates

This section presents the results obtained for the characterization of the Mg_2Si strengthening precipitates using SANS and TEM/HTEM. The SANS measurements were performed with the instrument SANS–2 at the German Engineering Materials Science Center (GEMS) in Geesthacht (Germany) in 2010. These tests were validated with TEM/HTEM analyses at the Helmholtz–Zentrum Geesthacht Center for Materials and Coastal Research.

Nanometer–scale Mg_2Si particles are the main strengthening precipitates that strengthen the general Al–Si–Mg alloy systems [6–9]. While the precipitation sequence has been extensively reported in the literature, emphasizing the first stages of nucleation and the formation of clusters from the decomposition of the supersaturated solid solution state of the alloy [12, 27, 28], the distributions of these Mg_2Si strengthening precipitates are still unknown.

The presence of copper in the alloy chemical composition due to its secondary nature leads to the formation of Al_2Cu strengthening precipitates. However, this element is present at a maximum of 0.3% in the alloy (Table 1) and is not considered to be responsible for the strengthening during the ageing process.

4.1 Small angle neutron scattering measurements

TEM is currently employed to study the evolution of the precipitation kinetics in this kind of alloy [12]. However, this procedure is not ideal due to the reduced material volume considered in the study, which is reduced to very thin foils. For cases where the objective is to analyze a relatively large volume leading to statistically meaningful results, scattering techniques that use synchrotron or neutron sources are ideal alternatives [29].

Despite the benefits of the small angle X–ray scattering procedure, such as its high resolution and short measurement time [30, 31], this technique has problems characterizing these nanometer–scale particles because both solutes (magnesium and silicon) involved in the nucleation, growth, and coarsening of these precipitates have a similar atomic number as the aluminum matrix, resulting in a negligible contrast between the matrix and the precipitates [29, 32]. SANS does not have this restriction and has thus been used to characterize the size distribution of the Mg_2Si strengthening precipitates present in this Al–Si–Mg alloy system. SANS principles can be easily found elsewhere, e.g., [33, 34].

4.1.1 Sample preparation and experiment

Disc–shaped samples (diameter 23 mm, thickness 3.5 mm) were prepared from the same original bar (bar length, 270 mm) casted as described (Sect. 3.1). These samples were heat–treated prior to performing the SANS measurements. Solution treatment at 535°C for 6 hours and quenching in water at room temperature were conducted for all of the samples before ageing them at 180°C, 210°C, 240°C, and 300°C for different times.

A neutron wavelength of 5.8 Å (wavelength spread of 10%) and different detector distances (mostly 1 m, 4.5 m, and 14.0 m) were used with appropriate collimators to cover the scattering vectors from 0.025 nm^{-1} to 3 nm^{-1} using unpolarized neutrons. The measured intensities were corrected for collecting transmission, background, and detector efficiency effects. Absolute cross–sections were obtained by calibrating against a Vanadium sample.

The macroscopic differential cross–section is calculated from the intensity measured by the detector I as [34]:

$$\frac{\mathrm{d}\Sigma}{\mathrm{d}\Omega} = \frac{I}{I_0 \cdot D \cdot \Delta\Omega \cdot T \cdot \eta} \ . \tag{2}$$

In Eq. (2), I is the measured intensity flux at the detector, I_0 is the primary beam intensity flux before being scattered, D is the sample thickness, $\Delta\Omega$ is the solid angle covered, T is the sample transmission, and η is the detector efficiency.

4.1.2 SANS Results

The neutron scattering cross–sections for the four ageing temperatures applied for different ageing times are presented in Fig. 6. These values agree with previous SANS investigations also performed for similar Al–Si–Mg alloy systems [9]. The scattering intensity curves exhibit the typical shoulder contribution at intermediate scattering vectors q of a unique distribution of strengthening precipitates of nanometer–scale (basically, β'– and β–Mg_2Si precipitates according to the precipitation kinetics [12, 27, 28]) for every ageing temperature with no cross–over at large scattering vectors q.

As the ageing time period is extended to smaller scattering vector q ranges, the shift of the characteristic shoulder confirms that nucleation, growth, and coarsening of the Mg_2Si strengthening precipitates are taking place during the artificial ageing stage. Therefore, the initial supersaturated solid solution of magnesium and silicon in the aluminum matrix is decomposed at the beginning of the artificial ageing, forming an initial β–Mg_2Si strengthening precipitate distribution that evolves to incoherent and coarse distributions as the ageing time increases. This evolution of these strengthening precipitates causes the mechanical properties of the alloy to deteriorate.

The obtained scattering curves are high quality. This feature happens because the artificial ageing treatments were selected before performing the measurements, which enables the use of long data acquisition times. If *in–situ* measurements are being taken, short time intervals (under 30 seconds) must be taken, such as when studying the first precipitation stages, because relatively fast changes in the precipitation are expected at the

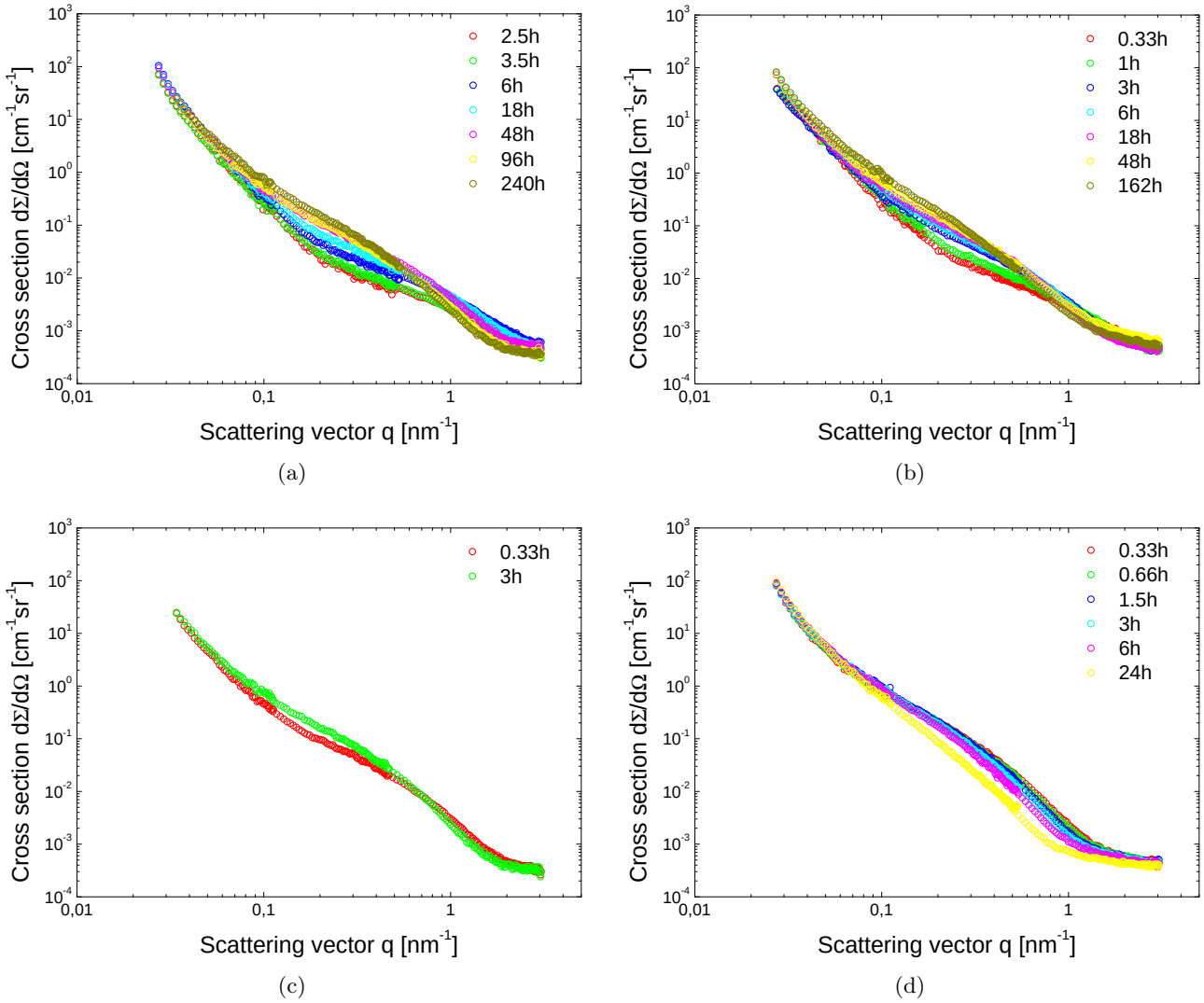

Figure 6: SANS scattering curves obtained from $AlSi_{10}Mg(Cu)$ samples artificial aged at: (a) 180°C for 2.5 h, 3.5 h, 6 h, 18 h, 48 h, 96 h, and 240 h; (b) 210°C for 0.33 h, 1 h, 3 h, 6 h, 18 h, 48 h, and 162 h; (c) 240°C for 0.33 h, and, 3 h; (d) 300°C for 0.33 h, 0.66 h, 1.5 h, 3 h, 6 h, and 24 h. Note that both axes are plotted on log-scales, and the x-axis is the reciprocal of dimensions in real space.

beginning of the artificial ageing process [29]. Additionally, the sample thickness of measured samples prevents multiple scattering from occurring.

At all of the ageing temperatures in this study, the scattering curves show a constant background using a large scattering vector q ($q = 4\pi \sin(\theta)/\lambda$, where 2θ is the scattering angle). For small scattering vectors q, larger structures, such as primary precipitates, inclusions, dispersoids, and grain boundaries, contribute to the effect. Larger structures contribute with a q^{-4}–tail in the visible q–range. For example, in the quenched state, where the material is at the supersaturated solid solution state, the scattering curves should be composed of a straight line q^{-4} contribution and a constant background at large scattering vector q values.

As the ageing time increases at every ageing temperature, the particle size distribution is expected to dramatically vary from the peak–aged states to the long over–aged ones according to the observed evolution of the scattering cross–sections.

4.1.3 Analysis of the size distribution of Mg_2Si strengthening precipitates

The measured scattering curves should be further analyzed in terms of the size and fraction of precipitates to fit the Robson simulation model for predicting these precipitate distributions, as shown in Sect. 5. The precipitates are assumed to have a rod–like shape, which was confirmed by the TEM images presented in Sect. 4.2. The local monodisperse approximation is adopted for the treatment of interparticle interference because the neutron scattering cross–sections show the characteristic shoulder caused by a high particle number density in the nanometer range [35]. In this approximation, the scattering cross–section of a dispersion of precipitate particles can be described by Eq. (3).

$$\frac{\mathrm{d}\Sigma}{\mathrm{d}\Omega}(q) = (\Delta\eta)^2 \cdot \int_0^\infty n(R)\, V(R)^2\, F(q,R)^2\, S(q,R,f) \cdot \mathrm{d}R \ , \tag{3}$$

where $\mathrm{d}\Sigma/\mathrm{d}\Omega$ is the macroscopic differential scattering cross–section, $\Delta\eta$ is the difference in the scattering length densities between particle and matrix, $n(R)\,\mathrm{d}R$ is the unknown size distribution of precipitates, $V(R)$ is the particle volume, $F(q,R)$ is the particle form factor, and $S(q,R,f)$ is the structure factor describing the interparticle interference effect [30].

Finally, the particle size distribution $n(R)$ is approximated by a normal distribution function of the radius:

$$n(R) = \frac{n_0}{\sqrt{2\pi}\sigma} \cdot \exp\left(-\frac{(R-R_0)^2}{2\sigma^2}\right) \ . \tag{4}$$

According to Eq. (4), the maximum and width of the distribution function, R_0 and σ, respectively, and the total density n_0 of the particles contained in the precipitate distributions at the different ageing states are determined by fitting a scattering curve calculated by Eq. (3) to the corresponding measured scattering curves shown in Fig. 6 using the least–squares procedure. This method is automatically computed using software developed by the GEMS Center. The results of this analysis are shown in Fig. 10.

4.2 Transmission electron microscopy

TEM/HTEM was used to determine the shape of precipitates and the preferred nucleation sites of the particles for fitting the precipitation model to predict the Mg_2Si strengthening precipitate distributions from the calculated cross–sections presented in Fig. 6 and to complement the results of the SANS measurements.

4.2.1 Sample preparation

Material from ageing state II (Table 2) was investigated using TEM/HTEM techniques. For these investigations, the material was cut by diamond saw, from which a 2.3 mm disc was drilled out and was subsequently ground to a thickness of approximatly 100 μm. This disc was thinned electrochemically using a solution of 33% HNO_3

with methanol at a temperature of −30°C. A voltage of 20 V was applied, generating a perforated specimen after approximately 1 minute with an average current of 80 mA during thinning.

4.2.2 TEM/HTEM Results

For TEM investigations, the specimen was tilted slightly to record all micrographs along the ⟨001⟩ zone axis of the aluminum matrix, in agreement with previously reported analyses of Mg_2Si precipitates [12]. HTEM micrographs of the aluminum matrix showed the expected atomic arrangement under this zone axis: a cubic lattice of atoms within the fcc aluminum. Fourier transformation of the micrographs gave maxima that reassembled the diffraction pattern of an unordered fcc crystal in the ⟨001⟩ orientation.

At a low magnification, elongated structures are visible in diffraction contrast in the specimen (Fig. 7(a)). They show no distinct contrast at atomic resolution but essentially retain the atomic structure of the aluminum matrix. From the high resolution pictures, it can be observed that, while distortion is present in the lattice, it is not caused by either a precipitate or by a coherent precipitate with equal crystallographic structure compared with the matrix.

Many small rod–shaped precipitates with a radius in the 5 to 10 nm range can be found in the peak–aged specimen. Two phase contrast images of Mg_2Si strengthening precipitates are shown in atomic resolution in Fig. 7(b). In this figure, when an objective aperture is applied, a diffraction contrast showing distortion of the aluminum matrix is visible. Nevertheless, this distortion contrast cannot directly be related to the precipitates.

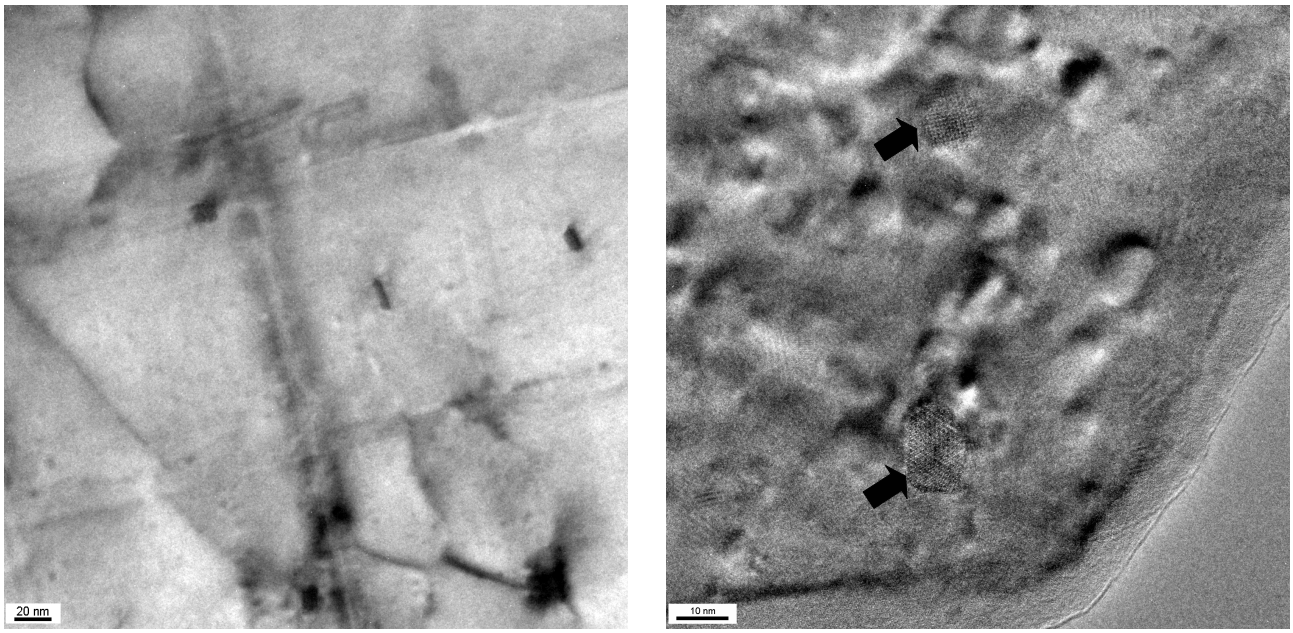

(a) (b)

Figure 7: (a) Atomic resolution micrograph of a rod–shaped coherent β''–Mg_2Si precipitate in the vicinity of an elongated structure with the same atomic structure as the aluminum matrix; (b) Atomic resolution filtered micrograph of two semi–coherent β'–Mg_2Si precipitates.

Higher magnification images of these precipitates reveal an atomic structure similar to those obtained for the

Mg_2Si phase in previous work [12], which corresponds to the thermodynamic metastable β' precipitate phase. However, the ultimate conclusion could only be drawn from simulations of the HTEM pictures. It is striking that the precipitates were not aligned with the atomic {001} layers of the aluminum matrix; rather, they deviated by approximately 10° (Fig. 8(a)), indicating that these precipitates were not fully coherent with the surrounding matrix, as is expected from metastable β'–Mg_2Si phases. However, the resolution is not sufficient to determine the continuity of the atomic layers at the interface.

Large precipitates were also present in the specimen (Fig. 8(b)). These large precipititates can be β'– or β–phase. It was not possible to generate pictures with atomic resolution for these structures. However, the crystallography is not cubic based on crystallography results, and implies that these large particles are not β–phase.

Finally, the precipitates and dislocations cannot be clearly correlated, implying that the nucleation of the precipitates takes place homogeneously throughout the aluminum matrix.

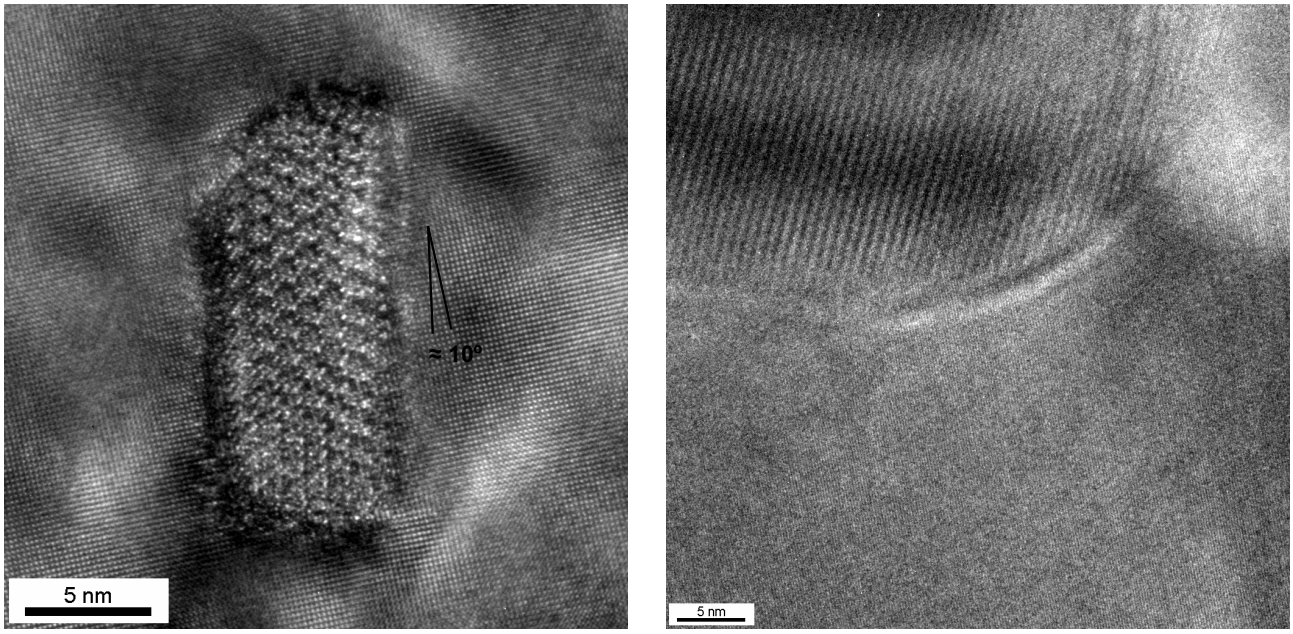

(a) (b)

Figure 8: (a) Atomic resolution micrograph of a semi–coherent β'–Mg_2Si precipitate. A deviation of approximately 10° with respect to the atomic {001} layers of the aluminum matrix is observed; (b) TEM micrograph of a large Mg_2Si precipitate.

5 Robson Model

Most of the simulation models used for predicting the precipitation process, such as the Johnson–Mehl-Avrami model [36] or the cluster dynamic model [37], are focused on the first stages of precipitation. Such models are unable to consider both the competitive growth and the coarsening processes of nucleated precipitates. Furthermore, the applicability and usefulness of these methods has been reported exclusively for isothermal ageing processes [38].

Conversely, there are models that take into account not only the nucleation and growth processes, but also the final coarsening stage when the matrix is depleted of solutes that contribute to strengthening precipitates, such as the original Langer and Schwartz model [39] and the Kampmann–Wagner numerical model [40]. Furthermore, these models are accurate enough to consider non–isothermal and complex artificial ageing treatments. The Kampmann–Wagner simulation model has been used to model the evolution of mechanical properties of Al–Si–Mg alloy systems during multi–step ageing [41]. However these simulation models for the evolution of the strengthening precipitates are fundamentally complicated and require a large amount of input data as well as a precise characterization and analysis of the precipitates. Consequently, these models are reduced to very specific alloy systems and precipitation processes.

5.1 Problem description and modeling objectives

Robson's numerical model consists of a nucleation model for the computation of the number of new precipitate nuclei formed at every step, a growth/dissolution rate for the previously nucleated particles, and a mass continuity equation of the solutes involved in the precipitation kinetics. This simulation model is suitable for dilute alloy systems [20].

This numerical precipitation model, which was further developed from the model proposed by Kampmann and Wagner [40], is used to predict the evolution of the equilibrium Mg_2Si strengthening precipitate distributions based on the temperature and ageing time conditions of the artificial ageing process. The model requires some simplifying assumptions, which are summarized as follows:

- Thermodynamically stable Mg_2Si strengthening precipitates present the stoichiometric composition. These are spherical–shaped precipitates with uniform thermodynamic properties.
- Mg_2Si strengthening particles are the only precipitate in which magnesium is significantly soluble.
- Nucleation of Mg_2Si precipitates is homogeneous within the aluminum matrix, as found in TEM investigations performed in Sect. 4.2 and also reported [25].
- The growth and coarsening of Mg_2Si strengthening particles are diffusion–controlled processes in which magnesium diffuses to the interface between the precipitates and the matrix.
- According to alloy composition, all of the magnesium is depleted into solution during the solution heat treatment. Magnesium is the limiting reagent, and silicon is present in excess.
- Because the diffusivity of magnesium and silicon solutes is similar at high temperatures [42], the solid solubility limits are obtained directly from a simple quasi–binary Al–Mg_2Si alloy system [43].

According to the formulated assumptions, it is possible to predict the growth and coarsening processes of the Mg_2Si precipitates without differentiating the characteristics of the different strengthening phases obtained during the precipitation sequence rather than needing to consider separate treatments for the β''–, β'–, and

the β–Mg_2Si phases because the precipitate curvature in the local composition of the interface between particle and matrix is taken into account. Therefore, the model allows the precipitation process to be simulated even for complex artificial ageing treatments by considering a dilute quasi–binary Al–Mg_2Si alloy and a simplified unique precipitate size distribution in which all of the new Mg_2Si precipitates nucleated are incorporated.

5.2 Mathematical modeling

The critical radius r^* of the particles nucleated in every new step is calculated using the Gibbs–Thomson equation in the singular case in which the concentration gradient at the interface between matrix and precipitates is exactly zero ($r = r^*$) [40], according to:

$$r^* = \frac{2\sigma V_a}{kT \ln \frac{c}{c_\infty^\alpha}} \ . \tag{5}$$

In Eq. (5), σ is the interfacial energy between the aluminum matrix and the Mg_2Si particles, V_a is the atomic volume of magnesium, k is the Boltzmann constant, T is the ageing temperature, c is the instantaneous concentration of magnesium in the matrix, and c_∞^α is the concentration of magnesium in the matrix in equilibrium with precipitates Mg_2Si assuming a planar interface.

From the calculated value of the critical radius r^*, the activation energy G^* required for the nucleation of new particles of the calculated size is computed according to [20]:

$$G^* = \frac{4}{3}\pi r^{*2} \cdot \sigma \ . \tag{6}$$

The activation energy G^* is added to the activation energy for the diffusion of magnesium in aluminum Q. Neglecting the incubation period, the steady–state nucleation rate J during artificial ageing is calculated by [44]:

$$J = N_0 \cdot \frac{kT}{h} \cdot \exp\left(-\frac{G^* + Q}{kT}\right) \ , \tag{7}$$

where N_0 is the number density of nucleation sites, and h is the Planck constant. In the case of homogeneous nucleation, the parameter N_0 is computed as the number of magnesium atoms per unit volume.

It can be inferred that the driving force for the nucleation process is the instantaneous concentration of magnesium c in the matrix. This stage of the precipitation process is consequently exhausted when the concentration of magnesium c is close to the equilibrium concentration c_∞^α at the corresponding temperature.

Similarly, for the nucleation phenomenon, the growth rate of the previously created Mg_2Si strengthening precipitates is calculated by assuming a diffusion controlled process in the case of spherical precipitates according to Eq. (8) [45]. This expression can be positive or negative, which requires the consideration of both growth and dissolution rates. At each calculation step, the precipitates that are larger than the calculated critical radius r^*

will grow and the smaller particles will shrink, corresponding to [39, 40]:

$$\frac{\mathrm{d}r}{\mathrm{d}t} = \frac{D}{r} \cdot \frac{c - c_r^{\alpha}}{c^{\alpha'} - c_r^{\alpha}} \ , \tag{8}$$

where D is the diffusion coefficient of magnesium in aluminum at a defined temperature, r is the discrete precipitate radius, c_r^{α} is the concentration of magnesium in the matrix at the interface and $c^{\alpha'}$ is the concentration of magnesium in the Mg_2Si precipitate. The parameter c_r^{α} is calculated for every particle radius from the generalized Gibbs–Thompson equation:

$$c_r^{\alpha} = c_{\infty}^{\alpha} \cdot \exp\left(\frac{2\sigma V_a}{kT} \cdot \frac{1}{r}\right) \ . \tag{9}$$

Finally, the dependence of the diffusion parameter D on the ageing temperature T is expressed according to the following Arrhenius–type equation:

$$D = D_0 \cdot \exp\left(-\frac{Q}{RT}\right) \ . \tag{10}$$

According to Eq. (5), the critical size calculated at every step r^* depends on the equilibrium magnesium content at the interface between the precipitate and the matrix, given by the phase diagram [46]. It is clear that the thermal stability of the precipitates depends on the changes in temperature during the ageing process. Thus, in the case of a non–isothermal ageing process, an increase in temperature leads to the dissolution of existing precipitates. Additionally, a decrease in the ageing temperature induces successive nucleation, growth, and coarsening of the precipitates. However, this phenomenon does not occur in these conditions because a single step ageing process at constant temperature was used.

Strengthening Mg_2Si nanometer–scale particles are supposed to cover the radius size range between 1 Å at nucleation and 1 μm for the long over–aged precipitates at long ageing times [1]. This radius size range has been divided into three hundred different classes using a logarithmic scale, thereby achieving a highly accurate tracking of the small precipitates, similar to previous implementations of Robson's model [3, 19]. At every time step, the nucleated precipitates calculated using Eq. (7) are placed in the corresponding size class according to the present critical radius r^* calculated from Eq. (5). Additionally, based on the growth/coarsening and their opposite processes for the previously nucleated particles, the increase/decrease of the size limits for all of the classes is calculated using Eq. (8). The initial distribution at the beginning of the increment is then reorganized. Once the new nucleated particles are placed and the existing ones have been redistributed, the remaining concentration of magnesium in the matrix c is computed. A schematic view of the implemented procedure for Robson's model is given in Fig. 9.

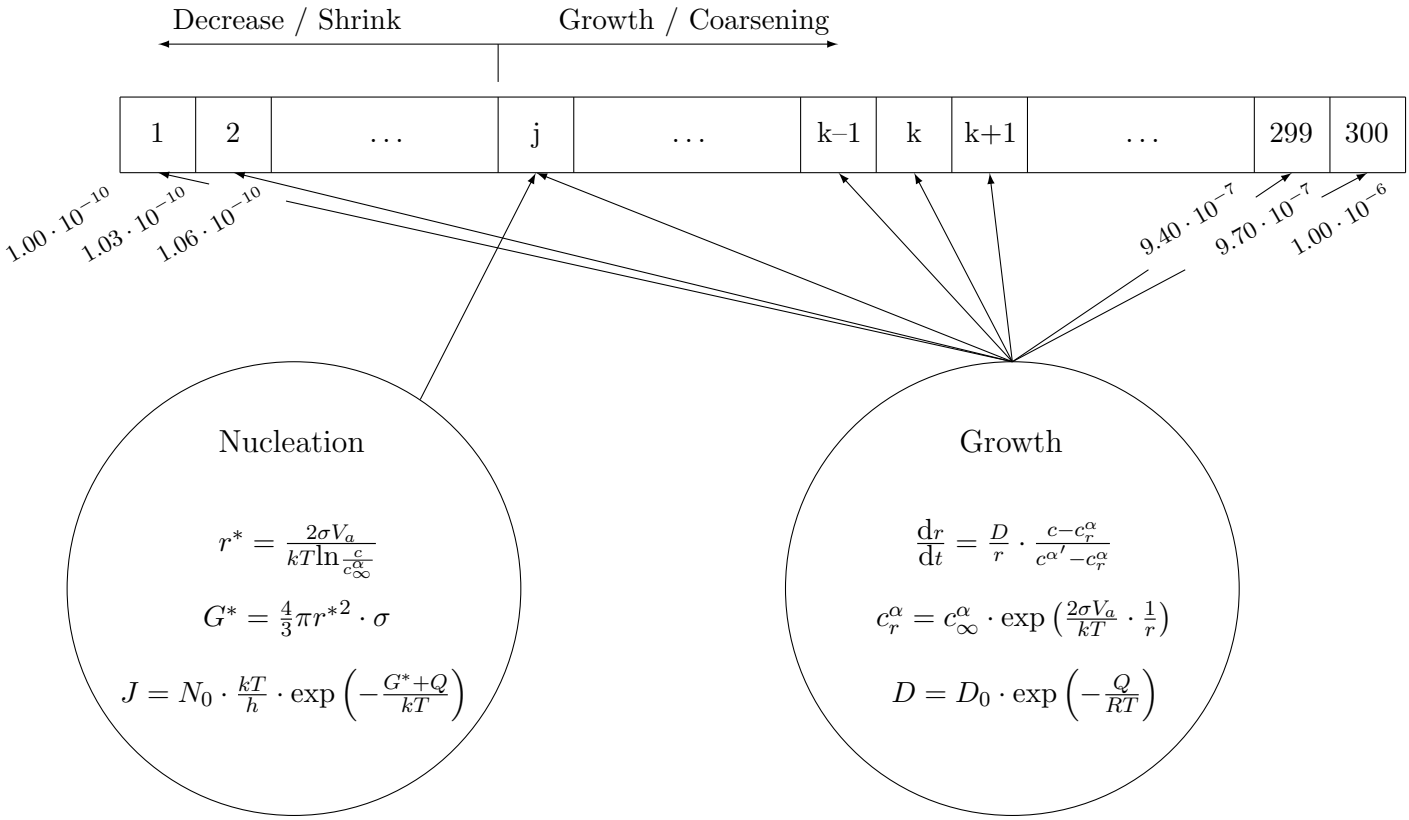

Figure 9: Method implemented to predict the evolution of the Mg_2Si strengthening precipitates during the artificial ageing process, assuming a size distribution of three hundred classes for the considered radius size range (0.1 nm — 1 μm).

5.3 Results

Fig. 10 presents the simulation results of the artificial ageing processes as described in Sect. 3.1 for the mean radius and the particle density of the Mg_2Si strengthening particles using Robson's model (Sect. 5.2). Four different ageing temperatures are considered, ranging from 180°C to 300°C. A good agreement between the SANS experimental measurements and the simulated results is obtained for the entire studied temperature range. The experimental data shown are based on assumptions made for the scattering intensity curves given in Fig. 6 as described in Sect. 4.1.3.

A high density of fine needle–shaped β''–Mg_2Si particles formed uniformly in the matrix during the first stages of artificial ageing at all temperatures (Fig. 10(b)). This phase is the dominant strengthening phase in the peak–aged T_6 heat treatment state of Al–Si–Mg alloys [12]. These fine, thermodynamically non–equilibrium precipitates will completely dissolve with increasing ageing temperature. Additionally, because the incubation period during nucleation is disregarded, the nucleation rate J is roughly constant and the density of the Mg_2Si precipitates grows at a constant rate in the first stages of precipitation where nucleation is the dominant phenomenon.

Fig. 10 also shows that at low ageing temperatures (T=180°C), there is no plateau in the growth of the precipitate mean radius when the Mg_2Si particle density reaches its maximum value, in contrast to predictions

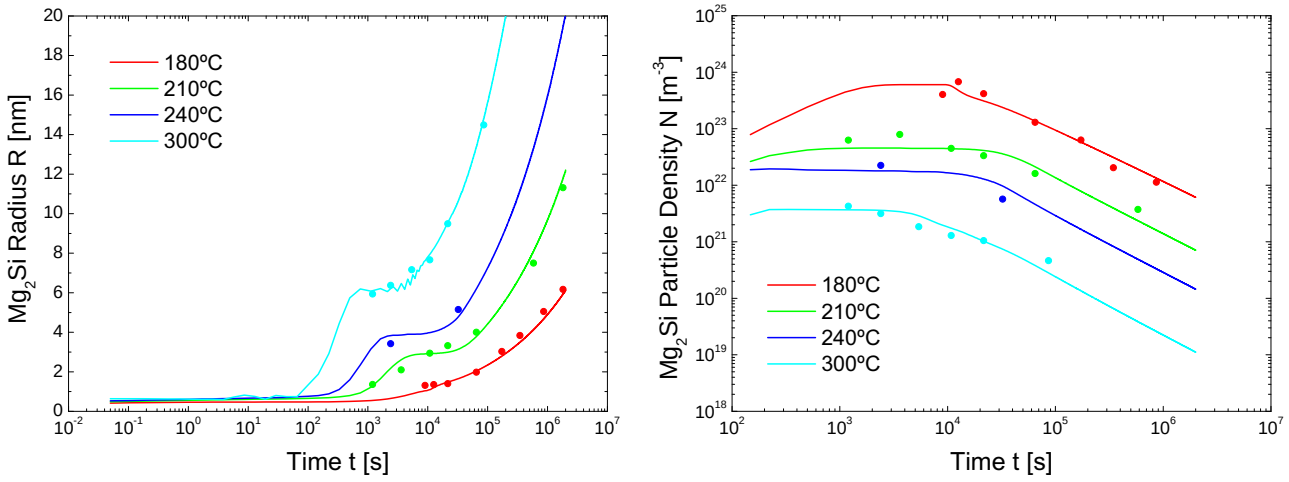

(a) (b)

Figure 10: Results of SANS measurements for the evolution of Mg_2Si strengthening particles and predictions using Robson's model for four different ageing temperatures 180°C, 210°C, 240°C, and 300°C referring to: (a) precipitate average size (note that the x-axis is plotted on a log-scale); (b) particle density (note that both axes are plotted on a log-scale). Note that straight lines correspond to predictions, while symbols represent experimental data.

at higher temperatures. This singular feature of the curve at 180°C is the consequence of a significant overlap between nucleation and coarsening, while for the other temperatures, the transition from nucleation to coarsening is more distinct. This phenomenon results from a low interfacial energy σ parameter that dominates in the class range of the majority of the strengthening precipitate distributions.

The double log–scale graph in Fig. 11 shows that the slope of all of the curves for the long ageing times (where coarsening of the strengthening distribution is taking place) is approximately 1/3, indicating that particle coarsening by Ostwald ripening dominates [47], confirming that large precipitates coarsen in the overageing process at the expense of the small ones when the matrix is depleted of the limiting solute. Thus, the overall energy in the material is reduced by a diffusion–driven process. This observation agrees well with the Lifshitz–Slyozov–Wagner (LSW) theory, which uses a kinetic equation appropriate for an infinitely dilute array of spherical particles in a stress–free matrix that predicts that the average particle radius will increase as a power function of the ageing time raised to 1/3 [48].

The governing driving force for coarsening is the difference between the matrix concentration in the vicinity of small and large particles, which leads to diffusion flux of the solute atoms from smaller particles to larger ones [49]. This phenomenon is caused by the Gibbs–Thomson effect included in the precipitation model, which changes the phase equilibrium between nanometer–scale precipitates and the matrix and also increases the solute concentration around small particles due to the interfacial curvature.

The input data used for Robson's model are listed in Table 4 with assumptions to simplify the problem. The Al–Si–Mg alloy system has been extensively examined, and the literature provides numerous examples from which the required parameters for the model can be extracted. It should be noted that the interfacial energy σ between the aluminum matrix and the Mg_2Si strengthening precipitates has been approximated by a sigmoidal

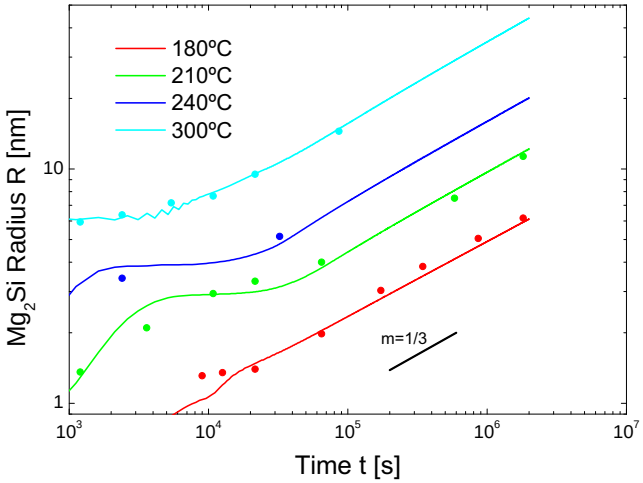

Figure 11: Evolution of the Mg_2Si strengthening precipitate size for four different ageing temperatures for long ageing times during which the Ostwald ripening coarsening process happens. Straight lines correspond to predictions, while symbols correspond to experimental data. Note that both axes are plotted on a log-scale.

function of the precipitate size as described in Sect. 5.3.1, while for previous reports it has been assumed to be constant [21]. The interfacial energy σ (that is, the sigmoidal function implemented for this parameter) and the diffusivity constant D_0 are the only two parameters fitted to SANS measurement data.

Parameter	Value	Units
N_0	$2.0239 \cdot 10^{24}$	part/m^3
Q	133000	J/mol
V_a	$3.95 \cdot 10^{-5}$	m^3/mol
σ	Sigmoidal function; Eq. (11)	J/mol
c_{ini}	0.41	wt %
$c^{\alpha'}$	63.4	wt %
D_0	$9.81 \cdot 10^{-5}$	m^2/s
$\rho_{\mathrm{AlSi_{10}Mg(Cu)}}$	2753	kg/m^3
ρ_{Mg_2Si}	1900	kg/m^3

Table 4: Input data for fitting the Robson precipitation model for the $AlSi_{10}Mg(Cu)$ alloy. The sigmoidal function parameter and the diffusivity constant D_0 have been fitted to the SANS measurement data.

In Table 4, the parameter c_{ini} is the concentration of magnesium in weight percentage present in the aluminum matrix at the supersaturated solid solution condition at the beginning of the precipitation process. This parameter coincides with the total concentration of magnesium in the alloy based on the simplifications made for modeling the process. The total concentration of magnesium in the material and the density of the $AlSi_{10}Mg(Cu)$ alloy $\rho_{\mathrm{AlSi_{10}Mg(Cu)}}$ have been measured at the laboratories of the Volkswagen AG. Note that the measured magnesium concentration falls within the established limits for the alloy composition given in Table 1.

5.3.1 Interfacial energy σ

The interfacial energy σ between formed precipitates and matrix for other aluminum alloys is not a constant, and some approximations have been successfully implemented in which this model parameter is directly dependent on the considered precipitates' size [22]. However, the applications of these approximations are reduced to very narrow and specific ranges of precipitate size and do not extend to the whole precipitation strengthening treatment. Additionally, the coarsening of the strengthening precipitates is usually accompanied by a loss of coherency in the matrix, so that an increase in the interfacial energy is also expected [50]. Extending this effect to the whole precipitation process implies that the transition from the very fine and coherent β''–Mg_2Si precipitates to the coarse and incoherent β–Mg_2Si strengthening particles should be accompanied by an increase in the interfacial energy σ. In fact, the assumption that the interfacial energy σ during the nucleation and the coarsening processes stays constant has been noted as a weakness in classical nucleation theory [22]. In this work, the interfacial energy σ needs to be a function of the precipitate size.

A transition from the lower value of σ, corresponding to the small nuclei, to the higher value for the coarse precipitates is included and agrees with previous investigations [22]. In this way, nucleation and coarsening can be correctly predicted. The quantitative value of this parameter assumes a characteristic rod shape for these particles and the interface created with the matrix. Under these assumptions, the selected function used to describe the dependence of the interfacial energy on the precipitate size $\sigma(r)$ is a generalized logistic function for modeling the growth of a magnitude [51]. The resulting interfacial energy function $\sigma(r)$ is shown in Fig. 12(a) and is given by the expression:

$$\sigma(r) = A + \frac{K - A}{\left(1 + Q \cdot \exp\left(-B \cdot (r - M)\right)\right)^{1/\nu}} \ , \tag{11}$$

where $A = 0.020$ is the lower asymptote, $K = 0.033$ is the upper asymptote, $Q = 45.0$ is fitted according to the value of $Y(0)$, $B = 8.75 \cdot 10^9$ is the growth rate, and $M = 8.0 \cdot 10^{-11}$ is the radius of maximum growth if $Q = \nu$. Parameter $\nu = 0.59$ denotes the place where maximum growth occurs.

Note that, in the assumptions made for Robson's model, the Mg_2Si strengthening precipitates are assumed to be spherical, which does not agree with the conclusions drawn from TEM images in Sect. 4.2. In fact, the intensity scattering curves obtained from the SANS measurements were analyzed for cylindrical particles. As a consequence, the size of the particles in Fig. 10 refers to the radius of the rod–shaped precipitates' cross–section.

5.3.2 Diffusivity constant D_0

The sensitivity of Robson's model to the diffusivity constant D_0 is also remarkable. This diffusion parameter has been identified from the discrete values of the diffusion constant D obtained from the individual fitting procedures done at every ageing temperature, assuming the activation energy for the diffusion of magnesium in aluminum Q given in Table 4. The parameter fitting results are shown in Fig. 12(b). The value for the

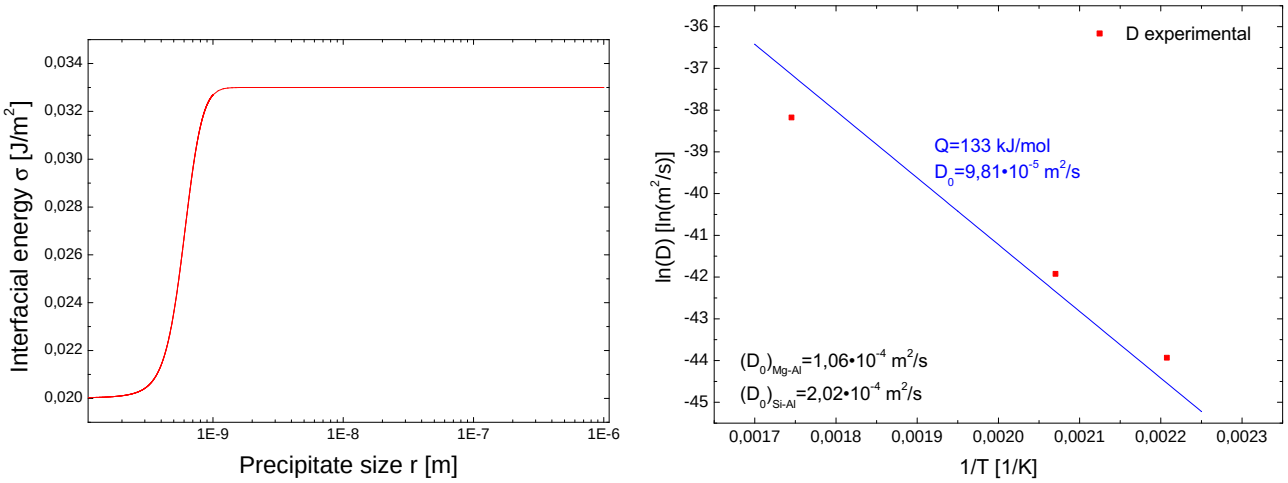

(a) (b)

Figure 12: Resulting fit of the material parameters of Robson's model: (a) interfacial energy as a function of the characteristic size of every precipitate class $\sigma(r)$ (note that x-axis is plotted on log-scale); (b) diffusivity constant D_0.

diffusivity parameter D_0 ($D_0 = 9.81 \cdot 10^{-5}$ m^2/s) is similar to values reported in the literature from experimental measurements ($D_0 = 10.6 \cdot 10^{-5}$ m^2/s) [42].

5.3.3 Solubility

The input data for the equilibrium concentration of magnesium c_∞^α are calculated using the projection of the magnesium concentration as the standard reference for the solid solubility. Table 5 gives the calculated equilibrium magnesium concentration c_∞^α at each temperature from the quasi–binary Al–Mg_2Si alloy system phase diagram [46].

Temperature	c_∞^α
K	wt %
453	0.1358
473	0.1585
513	0.1885
573	0.2328
673	0.3549

Table 5: The equilibrium concentration of magnesium c_∞^α in the matrix in equilibrium with Mg_2Si precipitates, assuming a planar interface for the temperature range of interest, as calculated from the quasi–binary Al–Mg_2Si phase diagram [46].

5.4 Outlook

The Robson model has been adapted to simulate the precipitation process of the Mg_2Si nanometer–scale strengthening particles of the $AlSi_{10}Mg(Cu)$ alloy system. Due to its physical fundamentals and the unique set of model parameters obtained, the model can be used to design the appropriate artificial ageing heat treatment processes by considering not only different ageing stages but also different heating and cooling rates. Thus, the model can be interpreted as an ideal tool for finding a compromise between the duration and temperature of the ageing process according to the required distributions of Mg_2Si strengthening precipitates to satisfy the mechanical demands of the application.

The adaptation of a constitutive mechanical model of simulation based on metal physics can be coupled with the predictions of the Mg_2Si strengthening precipitate distributions provided by Robson's model. The macroscopic mechanical response of the material to a loading history can then be easily simulated to establish a relationship between the results of the microstructure predictions and the parameters of the mechanical model. Moreover, the *in–situ* evolution of the mechanical properties in long duration, high temperature tests as a consequence of the changing size distribution of precipitates can also be predicted by coupling the models.

6 Conclusions

This work presents a comprehensive analysis of the microstructure of the age–hardenable $AlSi_{10}Mg(Cu)$ alloy and its evolution in the artificial ageing stage of a T_6–T_7 heat treatment process.

The nanometer–scale Mg_2Si strengthening precipitates formed in the artificial ageing state of the T_6 heat treatment process were found to be responsible for the observed changes in the mechanical behavior of the alloy. SANS was successfully used to characterize the precipitate distributions formed, providing good results with meaningful statistics. Four different ageing temperatures and ageing times were considered. Higher ageing temperatures produced coarser size distributions of Mg_2Si strengthening precipitates with a lower density. These investigations focused mainly on the intermediate growth and final coarsening processes.

TEM/HTEM was performed to verify the analysis of the Mg_2Si strengthening precipitates. The metastable β' and the thermodynamic equilibrium β phases of these precipitates had rod–like shapes. The formation of new precipitate nuclei takes place homogeneously in the aluminum matrix.

The Robson precipitation model was successfully fitted using the radii analysis and particle density obtained for the Mg_2Si strengthening precipitate distributions based on the SANS experimental data and the TEM analysis. The model was adapted to the present alloy system by considering only one precipitate size distribution for the different metastable and equilibrium Mg_2Si phases.

A unique set of parameters was used to predict the whole precipitation process and the whole range of temperatures using Robson's model. The interfacial energy parameter σ and the diffusivity constant D_0 were the two parameters fitted in the model. The model showed a high sensitivity to both values. The interfacial energy

parameter σ was explicitly dependent on the precipitate size. A sigmoidal approximation function was used to establish the dependency of the size of the precipitates $\sigma(r)$. The obtained value for D_0 was similar to experimental values reported in the literature.

Therefore, the size distributions of Mg_2Si strengthening precipitates were quantitatively characterized experimentally by testing different temperatures and durations of the artificial ageing process. The SANS data and TEM images allowed the successful adaptation of Robson's precipitation model. The adapted model correctly predicted the nucleation, growth, and coarsening stages of the Mg_2Si strengthening precipitate distributions with a simple procedure using a unique set of parameters. Moreover, the model successfully predicted the results for a wide range of ageing temperatures and different precipitation stages. These features make the model optimal for designing and optimizing complex non–isothermal artificial ageing processes for real precipitation heat treatment processes in industrial applications.

7 Acknowledgments

The authors wish to thank Prof. J. Mosler ✉ at Kiel University for his helpful discussions and supervision, the German Engineering Materials Science Center (GEMS) in Geesthacht, especially Mr. H. Eckerlebe ✉, for the critical SANS measurements, as well as the Helmholtz–Zentrum Geesthacht Center for Materials and Coastal Research for the general support.

8 Bibliography

[1] Abis S, Boeuf A, Caciuffo R, Fiorini R, Magnani M, Melone S, Rustichelli F, Stefanon M. J Nucl Mater 1985;135:181.

[2] Abis S, Caciuffo R, Coppola R, Magnani M, Rustichelli F, Stefanon M. Physica B 1986;136:469.

[3] Robson JD, Prangnell PB. Mater Sci Eng A-Struct 2003;352:240.

[4] Deschamps A, Solas D, Bréchet Y. Modeling of Microstructure Evolution and Mechanical Properties in Age–Hardening Aluminum Alloys, in: Bréchet Y (Ed.). Microstructures, Mechanical Properties and Processes - Computer Simulation and Modelling, Volume 3, first ed. Weinheim: Wiley–VCH Verlag; 1999.

[5] Thomas JJ, Verger L, Bignonnet A, Charkaluk E. Fatigue Fract Eng Mater Struct 2003;27:887.

[6] Moustafa MA, Samuel FH, Doty HW. J Mater Sci 2003;38:4507.

[7] Kliauga AM, Vieira EA, Ferrante M. Mater Sci Eng A-Struct 2008;480:5.

[8] Schiffmann R, Haug J, Banhart J. Int Conf Alum Alloy 2004;9:604.

[9] Albertini G, Caglioti G, Fiori F, Pastorelli R. Physica B 2000;276-278:921.

[10] Dieter GE. Mechanical Metallurgy, third ed. London: McGraw–Hill Book Company; 1986.

[11] Porter DA, Easterling KE. Phase Transformations in Metals and Alloys, second ed. London: Chapman & Hall; 1993.

[12] Edwards GA, Stiller K, Dunlop GL, Couper MJ. Acta Mater 1998;46:3893.

[13] Gupta AK, Lloyd DJ, Court SA. Mater Sci Eng A-Struct 2001;316:11.

[14] Tanaka M, Warner T. Rev Metall-Paris 2003;5:463.

[15] Fabregue D, Deschamps A, Suery M. Mater Sci Tech 2005;21:1329.

[16] Donnadieu P, Carsughi F, Redjaimia A, Diot C, Lapasset G. J Appl Crystallogr 1998;31:212.

[17] Seyedrezai H, Grebennikov D, Mascher P, Zurob HS. Mater Sci Eng A-Struct 2009;525:186.

[18] Ammar HR, Moreau C, Samuel AM, Samuel FH, Doty HW. Mater Sci Eng A-Struct 2008;489:426.

[19] Robson JD. Mater Sci Tech 2004;20:441.

[20] Robson JD. Acta Mater 2004;52:4669.

[21] Robson JD. Mater Sci Eng A-Struct 2004;382:112.

[22] Robson JD, Jones MJ, Prangnell PB. Acta Mater 2003;51:1453.

[23] Davis JR. Aluminum and Aluminum Alloys (ASM Specialty Handbook), first ed. Ohio: ASM International; 1993.

[24] Zhang B, Garro M, Leghissa M, Giglio A, Tagliano C. Proc SAE 2005 World Congr & Exhib 2005;M7.

[25] Falahati A, Lang P, Ahmadi M, Warczok P, Povoden-Karadeniz E, Kozeschnik E. Proc 6 Ranshofener Leichtmet 2010;6:61.

[26] Bruch E, Glatt W, Konzelmann W. Aluminium Gußlegierungen, Sekundär-Aluminium, Qualität und Recycling, first ed. Düsseldorf: Giesserei-Verl; 1988.

[27] Dutta I, Allen SM. J Mat Sci Lett 1991;10:323.

[28] Doan LC, Ohmori Y, Nakai K. Mat Trans JIM 2000;41:300.

[29] Staron P, Vaidya WV, Koçak M. Mater Sci Eng A-Struct 2009;525:192.

[30] Guinier A, Fournet G. Small Angle Scattering of X-rays, first ed. New York: Wiley; 1955.

[31] Glatter O, Kratky O. Small Angle X–ray scattering, first ed. London: Academic Press Inc; 1982.

[32] Deschamps A. Analytical Techniques for Aluminium, in: Totten GE, MacKenzie DS (Eds.). Handbook of Aluminium: Volume 2: Alloy Production and Materials Manufacturing, first ed. New York: Marcel Dekker Inc; 2003.

[33] Kostorz G. X–ray and neutron scattering, in: Cahn RW, Haasen P (Eds.). Physical Metallurgy: Volume 2, fourth ed. Amsterdam: Elsevier Science BV; 1996.

[34] Kostorz G. Treatise on Materials Science and Technology: Volume 15: Neutron Scattering, first ed. New York: Academic Press Inc; 1979.

[35] Pedersen J.S. J Appl Crystallogr 1994;27:595.

[36] Doherty RD. Nondiffusive phase transformations, in: Cahn RW, Haasen P (Eds.). Physical Metallurgy: Volume 2, fourth ed. Amsterdam: Elsevier Science BV; 1996.

[37] Mirold P, Binder K. Acta Metall 1977;25:1435.

[38] Bratland DH, Grong Ø, Shercliff H, Myhr OR, Tjøtta S. Acta Mater 1997;45:1.

[39] Langer JS, Schwartz AJ. Phys Rev A 1980;21:948.

[40] Kampmann R, Wagner R. Homogeneous Second Phase Precipitation, in: Cahn RW, Haasen P, Kramer EJ (Eds.). Materials Science and Technology: A Comprehensive Treatment, Volume 5 Phase Transformations in Materials, first ed. Weinheim, Wiley–VCH Verlag; 1991.

[41] Myhr OR, Grong Ø, Andersen SJ. Acta Mater 2001;49:65.

[42] Fujikawa SI. Defect Difuss Forum 1997;143-147:403.

[43] Nicolas M, Deschamps A. Acta Mater 2003;51:6077.

[44] Christian JW. The Theory of Transformations in Metals and Alloys (v.1–2), third ed. Oxford: Pergamon Press; 2002.

[45] Aaron HB, Fainstein D, Kotler GR. J Appl Phys 1970;41:4404.

[46] Hanemann H, Schrader A. Atlas Metallographicus Band III, Teil 2, Ternäre Legierungen des Aluminiums - Beispiele für die Kristallisation Ternärer Systeme, first ed. Düsseldorf: Verlag Stahl und Eisen; 1952.

[47] Gudladt HJ, Lendvai J, Schneider J. Acta Metall 1989;37:3327.

[48] Baldan A. J Mat Sci 2002;37:2171.

[49] Shahandeh S, Arami H, Sadrnezhaad SK. J Mat Sci 2007;42:9440.

[50] Novotny GM, Ardell AJ. Mater Sci Eng A-Struct 2001;318:144.

[51] Richards FJ. J Exp Bot 1959;10:290.